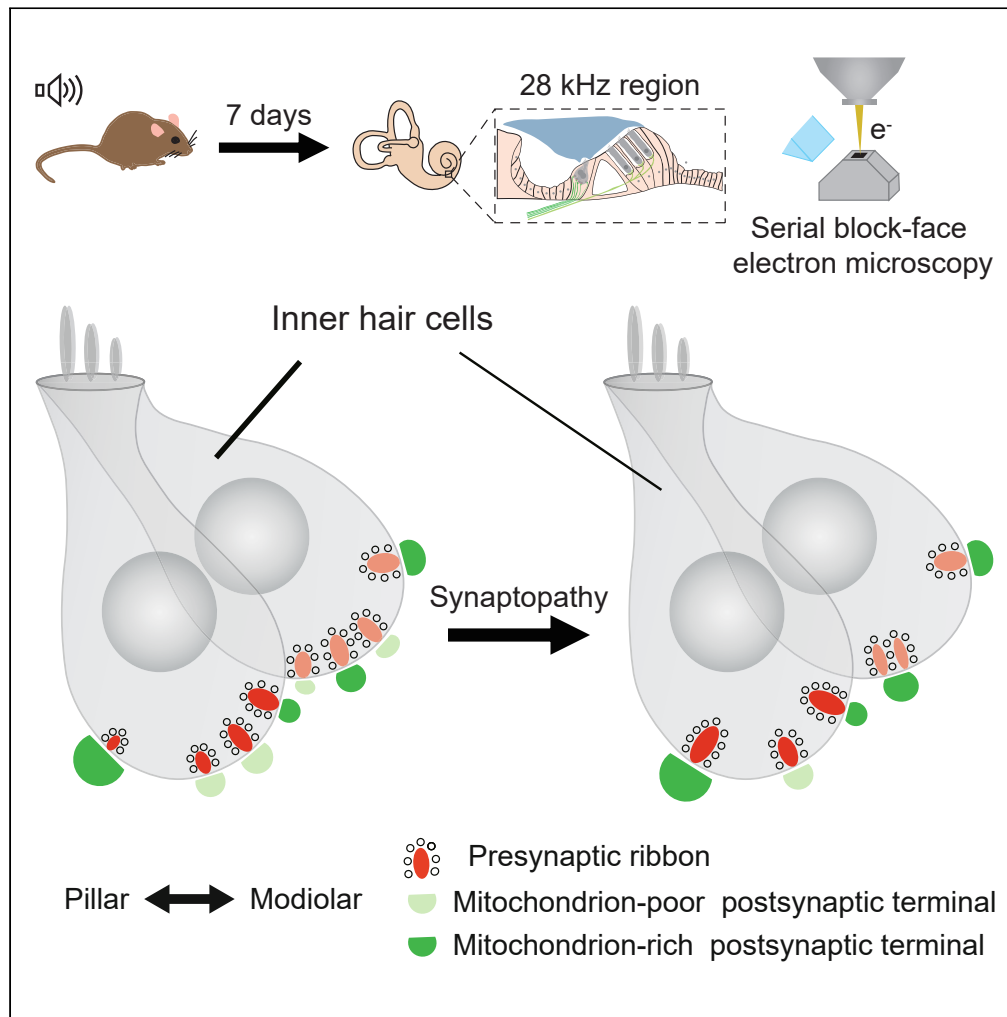


Article

# Spatial patterns of noise-induced inner hair cell ribbon loss in the mouse mid-cochlea



Yan Lu, Jing Liu, Bei Li, ..., Hao Wu, Hua Han, Yunfeng Hua

hua.han@ia.ac.cn (H.H.)  
yunfeng.hua@shsmu.edu.cn (Y.H.)

**Highlights**

Electron microscopic mapping of the noise-exposed mouse cochlea

Noise-induced spatial patterns of ribbon loss and morphological changes

Fewer mitochondrion-poor afferent nerve terminals after noise exposure



## Article

## Spatial patterns of noise-induced inner hair cell ribbon loss in the mouse mid-cochlea

Yan Lu,<sup>1,2,3,4,8</sup> Jing Liu,<sup>5,8</sup> Bei Li,<sup>1,2,3</sup> Haoyu Wang,<sup>4</sup> Fangfang Wang,<sup>4</sup> Shengxiong Wang,<sup>4</sup> Hao Wu,<sup>1,2,3,4</sup> Hua Han,<sup>5,6,7,\*</sup> and Yunfeng Hua<sup>1,2,3,4,9,\*</sup>

## SUMMARY

**In the mammalian cochlea, moderate acoustic overexposure leads to loss of ribbon-type synapse between the inner hair cell (IHC) and its postsynaptic spiral ganglion neuron (SGN), causing a reduced dynamic range of hearing but not a permanent threshold elevation. A prevailing view is that such ribbon loss (known as synaptopathy) selectively impacts the low-spontaneous-rate and high-threshold SGN fibers contacting predominantly the modiolar IHC face. However, the spatial pattern of synaptopathy remains scarcely characterized in the most sensitive mid-cochlear region, where two morphological subtypes of IHC with distinct ribbon size gradients coexist. Here, we used volume electron microscopy to investigate noise exposure-related changes in the mouse IHCs with and without ribbon loss. Our quantifications reveal that IHC subtypes differ in the worst-hit area of synaptopathy. Moreover, we show relative enrichment of mitochondria in the surviving SGN terminals, providing key experimental evidence for the long-proposed role of SGN-terminal mitochondria in synaptic vulnerability.**

## INTRODUCTION

The mammalian cochlea decomposes sounds into different frequency components by the basilar membrane (BM) to establish a place-frequency map for resident sensory epithelial cells—inner hair cells (IHCs)—as well as their postsynaptic spiral ganglion neurons (SGNs) (see reviews<sup>1–4</sup>). In rodents for instance, each IHC is contacted by about 20 predominantly unbranched peripheral dendrites of type I SGNs, forming almost the same number of active zones (AZs) with characteristic electron-dense and vesicle-tethering synaptic ribbons. These specialized connections are essential for ultrafast and temporally precise sound encoding. Early studies have revealed a characteristic spatial gradient with large ribbons on the modiolar (neural) IHC face whereas small ones on the pillar (abneural) face, and such morphological diversity of presynaptic ribbons is of functional importance. As the ribbon-bound synaptic vesicle (SV) pool increases with expanding ribbon volume,<sup>5</sup> the large synaptic ribbon can presumably supply more SVs rapidly down to the release site during sustained transmission, as recently observed in the retina.<sup>6,7</sup> Moreover, ribbons of different sizes are aligned to heterogeneous properties of the presynaptic Ca<sup>2+</sup>-channel clusters<sup>8,9</sup> as well as three distinct functional subtypes of SGNs.<sup>10–12</sup> A prevailing view on these diversified afferent connections is to enable collective neural encoding of the entire audible range by heterogeneous presynaptic Ca<sup>2+</sup>-influx-release coupling and the functionally fractionated SGNs (see reviews<sup>13–15</sup>).

In the mature cochlea, these fine-structured afferent connections are most susceptible to insults and non-regenerative once lost. On the 8-to-9-week-old CBA/CaJ mice, even moderate overexposure can lead to a permanent ribbon loss of up to ~50% and subsequent SGN death within a time span of two years.<sup>16,17</sup> As a causal consequence of ribbon loss (known as cochlear synaptopathy), coding deficits are probably implicated in weakened auditory discrimination under background noise, which is one of the hallmarks of “hidden hearing loss” (described as auditory neural processing disorder in subjects with normal audiometric thresholds) as well as presbycusis.<sup>18,19</sup> Extensive studies on the post-exposure dynamics of cochlear synaptopathy were conducted primarily using light microscopy in mice of different strains as well as guinea pigs (see reviews<sup>20,21</sup>). In the CBA/CaJ mice, large modiolar ribbons are found to be the first undergoing degeneration following noise exposure and in turn, the exposed IHCs lose their modiolar-pillar gradient in terms of ribbon size and abundance.<sup>17,22</sup> Although the exact mechanism of synaptopathy is still unclear, postsynaptic glutamate excitotoxicity is commonly believed to be an instigating factor.<sup>23–26</sup> In accordance with this view, the paucity of the terminal-resident mitochondria, as observed previously in the cat,<sup>27</sup> may account for the heightened

<sup>1</sup>Department of Otolaryngology-Head and Neck Surgery, Shanghai Ninth People's Hospital, Shanghai 200125, China

<sup>2</sup>Ear Institute, Shanghai Jiao Tong University School of Medicine, Shanghai 200125, China

<sup>3</sup>Shanghai Key Laboratory of Translational Medicine on Ear and Nose Diseases, Shanghai 200125, China

<sup>4</sup>Shanghai Institute of Precision Medicine, Ninth People's Hospital, Shanghai Jiao Tong University School of Medicine, Shanghai 200125, China

<sup>5</sup>Laboratory of Brain Atlas and Brain-inspired Intelligence, Institute of Automation, Chinese Academy of Sciences, Beijing 100190, China

<sup>6</sup>School of Future Technology, University of Chinese Academy of Sciences, Beijing 101408, China

<sup>7</sup>State Key Laboratory of Multimodal Artificial Intelligence Systems, Institute of Automation, Chinese Academy of Sciences, Beijing 100190, China

<sup>8</sup>These authors contributed equally

<sup>9</sup>Lead contact

\*Correspondence: [hua.han@ia.ac.cn](mailto:hua.han@ia.ac.cn) (H.H.), [yunfeng.hua@shsmu.edu.cn](mailto:yunfeng.hua@shsmu.edu.cn) (Y.H.)

<https://doi.org/10.1016/j.isci.2024.108825>



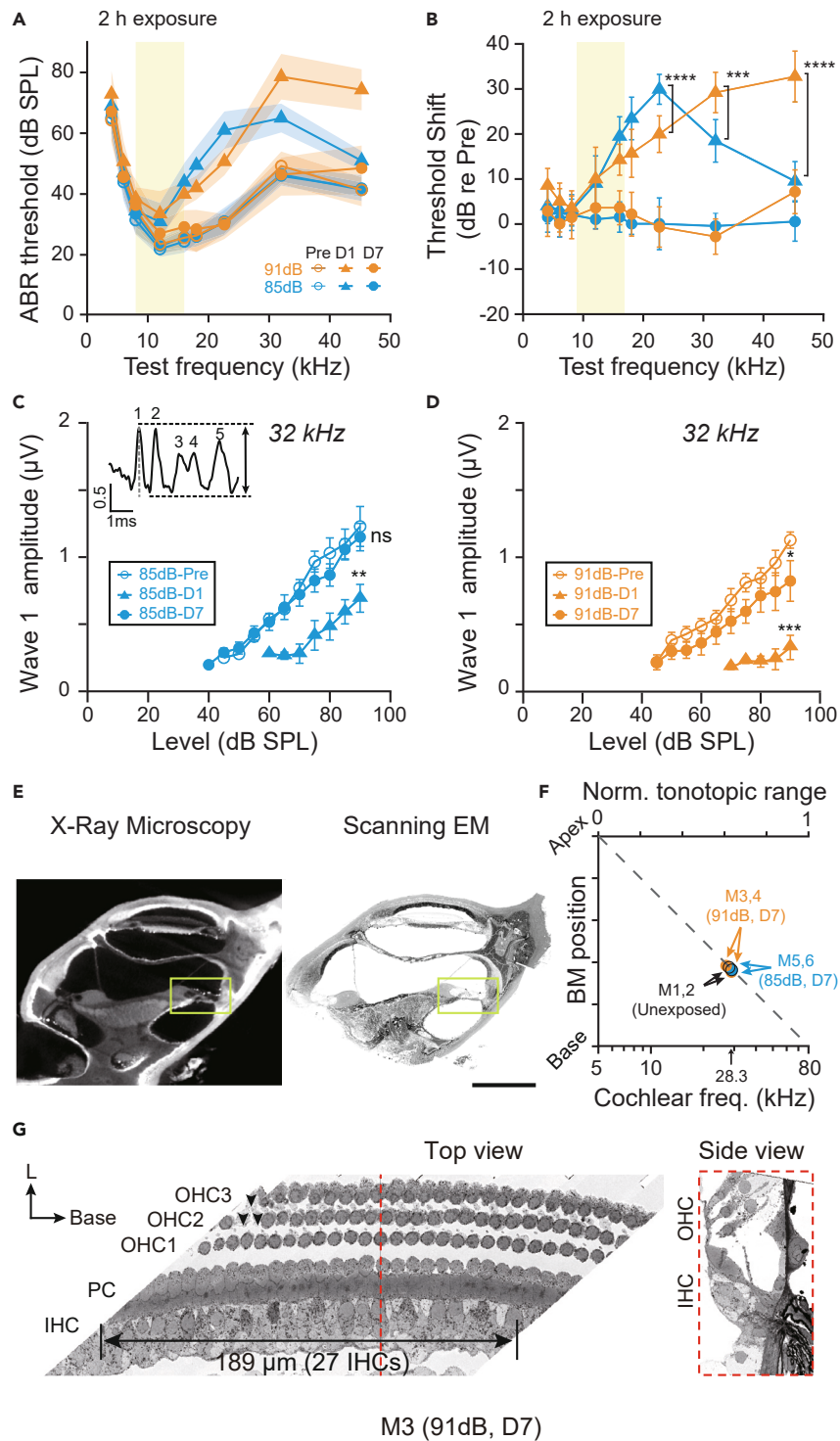


**Figure 1. SBEM imaging of noise-exposed cochlea**

(A) Both 85-dB (blue,  $n = 10$  animals) and 91-dB (orange,  $n = 7$  animals) exposures produced a transient elevation in hearing thresholds on post-exposure day one (D1, triangles) which was fully recovered on post-exposure day seven (D7, filled circles) in comparison with the baseline values before exposure (Pre, empty circles).

(B) Relative ABR threshold shifts computed from (A). Different threshold shifts on D1 after the 85-dB (blue) and the 91-dB (orange) exposures at the best-frequencies of 22.6 kHz ( $30.00 \pm 1.05$  dB vs.  $20.00 \pm 0.99$  dB, two-sample t test, \*\*\*\* $p < 0.0001$ ), 32 kHz ( $18.50 \pm 1.50$  dB vs.  $29.29 \pm 1.09$  dB, \*\*\* $p = 0.0003$ ), and 45.2 kHz ( $9.50 \pm 1.38$  dB vs.  $32.86 \pm 1.38$  dB, \*\*\*\* $p < 0.0001$ ).

**Figure 1. Continued**

(C) ABR-wave-1 amplitude (inset) growth function in the 32 kHz cochlear region before (Pre, open circles), on D1 (triangles), and D7 (filled circles) after the 85-dB exposure. In comparison with the baseline values (Pre,  $1.2283 \pm 0.1486 \mu\text{V}$ ), a temporary decline in neural response amplitude is observed on D1 ( $0.6931 \pm 0.1037 \mu\text{V}$ ) but not on D7 ( $1.1492 \pm 0.1022 \mu\text{V}$ ) upon a 90-dB test stimulus. Paired-sample t-test,  $p = 0.0042$  (Pre vs. D1),  $p = 0.5883$  (Pre vs. D7).

(D) Same as (C), only partial recovery of the ABR-wave-1 amplitude on the post-91-dB exposure D7 (filled circles,  $0.8240 \pm 0.1512 \mu\text{V}$ ) from D1 (triangles,  $0.3288 \pm 0.0903 \mu\text{V}$ ) was observed, compared to the unexposed controls (Pre, open circles,  $1.1276 \pm 0.0600 \mu\text{V}$ ). Paired-sample t-test,  $p = 0.0004$  (Pre vs. D1),  $p = 0.0499$  (Pre vs. D7).

(E) Representative example of structural matching between X-ray microscopic virtual section (left) and the block-face imaged by SBEM (right) with the target location indicated by green box. Scale bar,  $500 \mu\text{m}$ .

(F) Relative BM locations determined for individual SBEM volumes (unexposed control group: black empty circles; the 85-dB group: blue filled circles; the 91-dB group: orange filled circles), which were used to infer the best-frequencies of the SBEM-imaged IHCs based on a normalized tonotopic range from 5 to 80 kHz. This yielded a mean frequency of  $28.3 \pm 0.9 \text{ kHz}$  for the acquired datasets.

(G) Example SBEM virtual horizontal (left) and sagittal sections (right) of the organ of Corti (M3). Dashed line represents the location of the side view. (Left) Rows of inner hair cells (IHC), outer hair cells (OHC1, OHC2, OHC3), and pillar cells (PC) are indicated. Black arrows mark the three missing OHCs (two in OHC2 and one in OHC3). Data in (B), (C), and (D) are presented as mean  $\pm$  SEM. Data in (F) are presented as mean  $\pm$  SD.

vulnerability of SGN terminals contacting the modiolar IHC face, perhaps owing to the limited capacity of  $\text{Ca}^{2+}$  uptake during sustained synaptic transmission. However, this notion remains speculative because the fact that there are fewer mitochondria in the low spontaneous-rate SGN fibers has been demonstrated so far only in the cat<sup>27,28</sup> and noise-induced synaptopathy has been suggested not as selective as originally expected.<sup>29</sup>

Recent studies in mice of different strains<sup>30–32</sup> have documented the coexistence of two IHC subpopulations with a staggering of their basolateral pole positions in the mouse mid-cochlear region (6–32kHz). Strikingly, the type-A IHC (long cell body) with a basolateral pole tilting more toward the pillar cell appears to have larger and more ribbons on the modiolar IHC face. On the contrary, the type-B IHC (short cell body) that is closer to the modiolus contains exclusively large ribbons gathering predominantly on the pillar face.<sup>31</sup> Given distinct size gradients and spatial distributions of ribbons in these two IHC morphological subtypes, emerging questions arise about how noise-induced synaptopathy would impact type-A and type-B IHCs and whether the long-standing dogma of postsynaptic excitotoxicity still holds.

Now technical advances in volume electron microscopy have enabled the reconstruction of IHCs at unprecedented large scale and superior resolution.<sup>5,31–34</sup> To address the aforementioned questions, we employed serial block-face scanning electron microscopy (SBEM) for an ultrastructural analysis on six large cochlea datasets acquired from juvenile CBA/Ca mice with or without acoustic overexposure history. This reveals mixed spatial patterns in terms of ribbon morphology in type-A and type-B IHCs following either synaptopathic or non-synaptopathic noise exposure. Besides, by comparing experimental data and model inference, we obtained circumstantial evidence for the determinant role of mitochondrial content in the SGN survival upon noise insult.

## RESULTS

### SBEM imaging of noise-exposed cochlear organ of corti

In this study, we used a 2-h-long (2h) octave-band noise (8–16 kHz) to induce temporary hearing loss in male CBA/Ca mice at five weeks of age. In line with previous observations,<sup>16,17,35</sup> upon the so-called synaptopathic (91-decibels, 91-dB, 2h) as well as non-synaptopathic (85-dB, 2h) sounds, auditory brainstem responses (ABRs) of the exposed animals exhibit transient hearing threshold elevations with distinct frequency characters (Figures 1A and 1B). Specifically, the peak threshold elevation of the non-synaptopathic group (85-dB) was at 22.6 kHz on post-exposure day one (D1), while the synaptopathic group (91-dB) featured a monotonically increased threshold elevation with the frequency starting from 8 kHz and reaching a maximum at 45.2 kHz. On post-exposure day seven (D7), a full recovery in the ABR thresholds was observed in both groups (Figures 1A and 1B). Note that our juvenile (5–6 weeks) CBA/Ca mice appear to be more susceptible to moderate noise exposure than mature animals (>8 weeks). To the best of our knowledge, such age-related difference in the temporary hearing loss has not been reported (see Discussion). The cochlear synaptopathy is confirmed by an irreversible reduction in the ABR-wave-1 amplitudes observed on D7 only in the 91-dB exposed group (Figures 1C and 1D). From the cohort, we collected cochlea tissues from six individual animals on the experimental D7 (postnatal day 42, p42, see Table 1 for more information). To instruct sample trimming for SBEM and post-hoc determine the frequency range of the acquired SBEM volume, non-destructive tomographic scans of the embedded whole cochlea samples were performed using X-ray microscopy (Figures 1E and S1). Six SBEM volumes were taken from the mid-basal cochlear region with an estimated frequency range of  $28.3 \pm 0.9 \text{ kHz}$  (Figure 1F), among which two were from animals (M1, 2) without noise-exposure history, whereas the others were from animals experiencing single exposure to either 91-dB (M3, 4) or 85-dB noise (M5, 6). Consistent with prior light microscopy (LM) studies, almost no loss in cochlear hair cells, especially noise-vulnerable outer hair cells (OHCs), is observed in these datasets (Table 1). In the only case (Figure 1G, M3), we noted three missing OHCs out of 79 on D7.

### Enlarged and multi-ribbons after acoustic overexposure

We volume reconstructed 122 intact IHCs and all 1894 ribbon synapses in the SBEM datasets (Figure 2A; Table 1). In good agreement with LM studies,<sup>16,17,35,36</sup> a substantial ribbon loss (29.4%) was observed in the 28 kHz cochlear region of the synaptopathic ears in comparison with the unexposed control as well as the non-synaptopathic groups (Figure 2B; Table 1). Upon synaptopathy, the IHCs tend to have larger ribbons than those of the unexposed IHCs as well as the exposed IHC without ribbon loss (Figure 2C; Table 1). Since we did not observe an

**Table 1. Six SBEM datasets acquired from CBA/Ca mice**

	M1	M2	M3	M4	M5	M6
Sex & age (group)	Male, p42 (UE)	Male, p42 (UE)	Male, p42 (D7)	Male, p42 (D7)	Male, p42 (D7)	Male, p42 (D7)
Noise exposure	Unexposed	Unexposed	8-16 kHz, 91dB,2h	8-16 kHz, 91dB,2h	8-16 kHz, 85dB,2h	8-16 kHz, 85dB,2h
Change of ABR-wave-1 amplitude ( $\mu\text{V}$ ) <sup>a</sup>	–	–	0.3145	0.2849	0.0919	0.0933
Cochlear frequency (kHz)	27.8	28.3	26.9	29.4	28.2	29.0
Resolution ( $\text{nm}^3$ )	12 × 12 × 50	12 × 12 × 50	12 × 12 × 50	12 × 12 × 50	11 × 11 × 50	11 × 11 × 50
Volume ( $\mu\text{m}^3$ )	148 × 295 × 154	124 × 302 × 128	128 × 360 × 139	125 × 251 × 146	237 × 119 × 155	136 × 269 × 123
Number of IHCs (type-A/type-B)	15 (9/6)	18 (12/6)	26 (16/10)	20 (14/6)	24 (13/11)	19 (13/6)
Number of OHCs (OHC1/2/3)	16/16/16	19/18/19	27/24 <sup>b</sup> /25 <sup>c</sup>	22/22/22	23/22/23	18/18/20
Ribbon counts/IHC <sup>d</sup>	17.9 ± 2.0	16.3 ± 1.6	11.6 ± 3.4	12.5 ± 1.9	19.0 ± 1.9	17.2 ± 1.7
Ribbon volume/active zone ( $\mu\text{m}^3$ ) <sup>e</sup>	0.0132 ± 0.0063	0.0124 ± 0.0064	0.0157 ± 0.0091	0.0194 ± 0.0089	0.0142 ± 0.0059	0.0144 ± 0.0054

<sup>a</sup>Relative to Pre.

<sup>b</sup>Two missing OHCs in the second row.

<sup>c</sup>One missing OHC in the third row.

<sup>d</sup>Data are represented as mean ± SD.

<sup>e</sup>Data are represented as mean ± SEM.

increased occurrence of ribbon hollowing (translucent cores inside the ribbons) on D7 in the exposed ears (Figure S2A), this ribbon enlargement may reflect putative activity-dependent plasticity change. As multiple ribbons can be found in one AZ, the ribbon volume per AZ can be evaluated by pooling all ribbons from each AZ. We then compared the cumulative distribution of ribbon volume on pooled AZs and found a reduced population of single small ribbons in both exposed groups (Figure 2D). In addition, IHCs of the synaptopathic group (91dB) appear to have a higher occurrence of multi-ribbon AZs (Figure S2B), resulting in not only more oversized ribbons but also a broader ribbon size distribution (Figure 2D). Together, these results reveal ultrastructural insights into the adaptive plasticity of presynaptic ribbons.

### Differential synaptopathy in the exposed IHCs

All six datasets from the 28 kHz cochlear region contain morphologically distinct IHCs with staggered positions of their basolateral poles (Figure 3A). We determined the tilt angles of each IHC relative to the middle plane between IHC pairs ( $0^\circ$ ), allowing a clear partition into the type-A and type-B IHCs (Figure 3B; Table 2). The type-A IHCs, which are more tilted toward the pillar cells, appear to have longer cell bodies than their type-B counterparts (type-A IHCs: filled circles,  $35.97 \pm 2.74 \mu\text{m}$ ; type-B IHCs: empty circles,  $32.43 \pm 2.83 \mu\text{m}$ ; Two-sample t test:  $p < 0.0001$ ). The ribbon counts suggest a homogeneous synaptopathy across all the reconstructed type-A IHCs, meanwhile nearly half of the type-B IHCs show a greater reduction in ribbon synapses (Figure 3C). This effect can be consistently observed from the resultant inter-IHC subtype difference in ribbon counts concomitant with the synaptopathy (Figure S3). Given that neighboring IHCs receive almost the same dose of noise exposure, this result indicates the heightened vulnerability of ribbon synapses in type-B (short) IHCs.

Next, we compared the type-A and type-B IHCs in respect of their spatial pattern of synaptopathy (Figure 3D; Table 2). In the type-A IHCs, ribbon loss occurs exclusively on the modiolar face, where the SGN terminals are more densely packed under normal condition. By contrast, the pillar ribbons of type-A IHCs appear noise damage-resistant. In the case of type-B IHC, the modiolar ribbons are fewer in number but more robust to synaptopathy than those on the pillar side, among which loss of a significant portion is deduced based on ribbon counts. Intriguingly, the noise-related ribbon enlargement appears to impact the type-A IHCs on not only the modiolar face but also the pillar face, where no ribbon loss was observed (Figure 3E; Table 2). Thus, the prominent ribbon size gradient is effectively compromised by eliminating large modiolar ribbons and making small pillar ribbons bigger. As to the type-B IHCs, the overweighed synaptopathy and ribbon enlargement are both found on the pillar IHC face (Figure 3E). Finally, we quantified the synapse density by measuring the mean inter-ribbon distances (Figure 3F; Table 2). The result suggests that synaptopathy makes the ribbon synapses alienated from each other on the modiolar face of type-A IHC and diminishes the ribbon density gradient along the IHC modiolar-pillar axis. Unexpectedly, in the type-B IHCs, this gradient appears to be maintained despite a substantial ribbon loss.

In summary, we report that the noise-related ribbon loss takes place preferentially on the modiolar side of type-A IHC and the pillar side of type-B IHC (Figure 3D). These regions coincide with those of the highest SGN innervation density (Figure 3F) and feature enlarged ribbons upon synaptopathy (Figure 3E). Note that the pillar ribbons of type-A IHC seem to undergo activity-dependent enlargement as well (Figure 3E), arguing for an IHC-wide plasticity change of ribbons in addition to local synaptic reorganization. These observations enrich our current view of noise-induced cochlear damage by revealing a set of differences in the spatial patterns of synaptopathy between two IHC morphological subtypes.

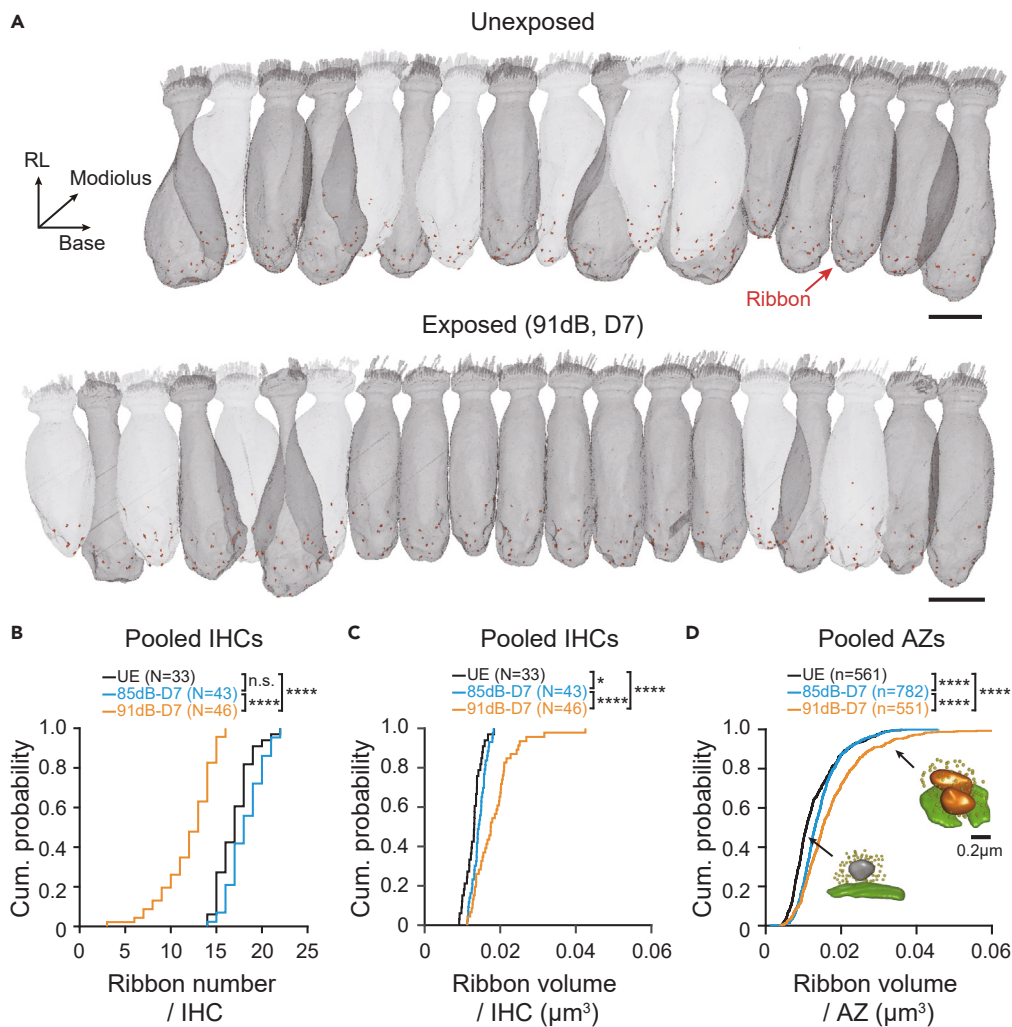


**Figure 2. Fewer and larger IHC ribbons after the noise exposures**

(A) For illustration, volume rendering of 18 reconstructed IHCs (gray) and 20 reconstructed IHCs (gray) from the unexposed and the 91-dB exposed group (91dB, D7). Red dots at the IHC basolateral surface represent the synaptic ribbons. Scale bar, 20  $\mu\text{m}$ .

(B) Cumulative probability distribution of ribbon numbers from pooled IHCs of the noise-exposed (85dB and 91dB) and unexposed (UE) ears. The median and mean ribbon numbers are 17.0 and  $17.0 \pm 1.9$  (UE), 18.0 and  $18.2 \pm 2.0$  (85dB), 13.0 and  $12.0 \pm 2.9$  (91dB). Two-sample Kolmogorov-Smirnov test:  $p = 0.1346$  (UE vs. 85dB),  $p < 0.0001$  (85dB vs. 91dB), and  $p < 0.0001$  (UE vs. 91dB).

(C) Same as (B), but with ribbon size from pooled IHCs. The median and mean ribbon volumes are  $0.0131 \mu\text{m}^3$  and  $0.0129 \pm 0.0004 \mu\text{m}^3$  (UE),  $0.0143 \mu\text{m}^3$  and  $0.0144 \pm 0.0003 \mu\text{m}^3$  (85dB),  $0.0175 \mu\text{m}^3$  and  $0.0184 \pm 0.0008 \mu\text{m}^3$  (91dB). Two-sample Kolmogorov-Smirnov test:  $p = 0.0100$  (UE vs. 85dB),  $p < 0.0001$  (85dB vs. 91dB), and  $p < 0.0001$  (UE vs. 91dB).

(D) Same as (B), but with ribbon size from pooled AZs. The median and mean ribbon volumes are  $0.0108 \mu\text{m}^3$  and  $0.0128 \pm 0.0064 \mu\text{m}^3$  (UE),  $0.0130 \mu\text{m}^3$  and  $0.0143 \pm 0.0057 \mu\text{m}^3$  (85dB),  $0.0151 \mu\text{m}^3$  and  $0.0174 \pm 0.0092 \mu\text{m}^3$  (91dB). Two-sample Kolmogorov-Smirnov test:  $p < 0.0001$  (UE vs. 85dB),  $p < 0.0001$  (85dB vs. 91dB), and  $p < 0.0001$  (UE vs. 91dB). Data in (B) and (D) are presented as mean  $\pm$  SEM. Data in (C) are presented as mean  $\pm$  SD.

### Characterizing mitochondrial content in the SGN terminals

Early electron microscopy (EM) study in the cat has shown that low spontaneous-rate (SR) SGN dendrites contact exclusively the modiolar IHC face via small and mitochondrion-poor terminals.<sup>27</sup> Similarly, in our SBEM datasets of the mouse cochlea, both mitochondrion-rich/poor SGN terminals can be identified (Figure 4A). Next, we set out to explore potential correlation between the postsynaptic difference in mitochondrial content and the mixed spatial pattern of synaptopathy in the type-A/B IHCs. For that, the numbers of mitochondria were counted manually in the SGN terminals of both unexposed and recovered ears (Figures 4B–4D). In line with early observation on the cat, type-A IHC of the mouse is innervated preferentially by mitochondrion-poor SGN terminals on the modiolar face (Figure 4B). By contrast to type-A IHC, the nerve terminals on type-B IHC are mitochondrion-rich and do not show a modiolar-pillar gradient (Figure 4B). A nearly identical pattern with respect to the postsynaptic mitochondrial content was observed in the 85-dB exposed group (Figure 4C), suggesting limited mitochondrial plasticity

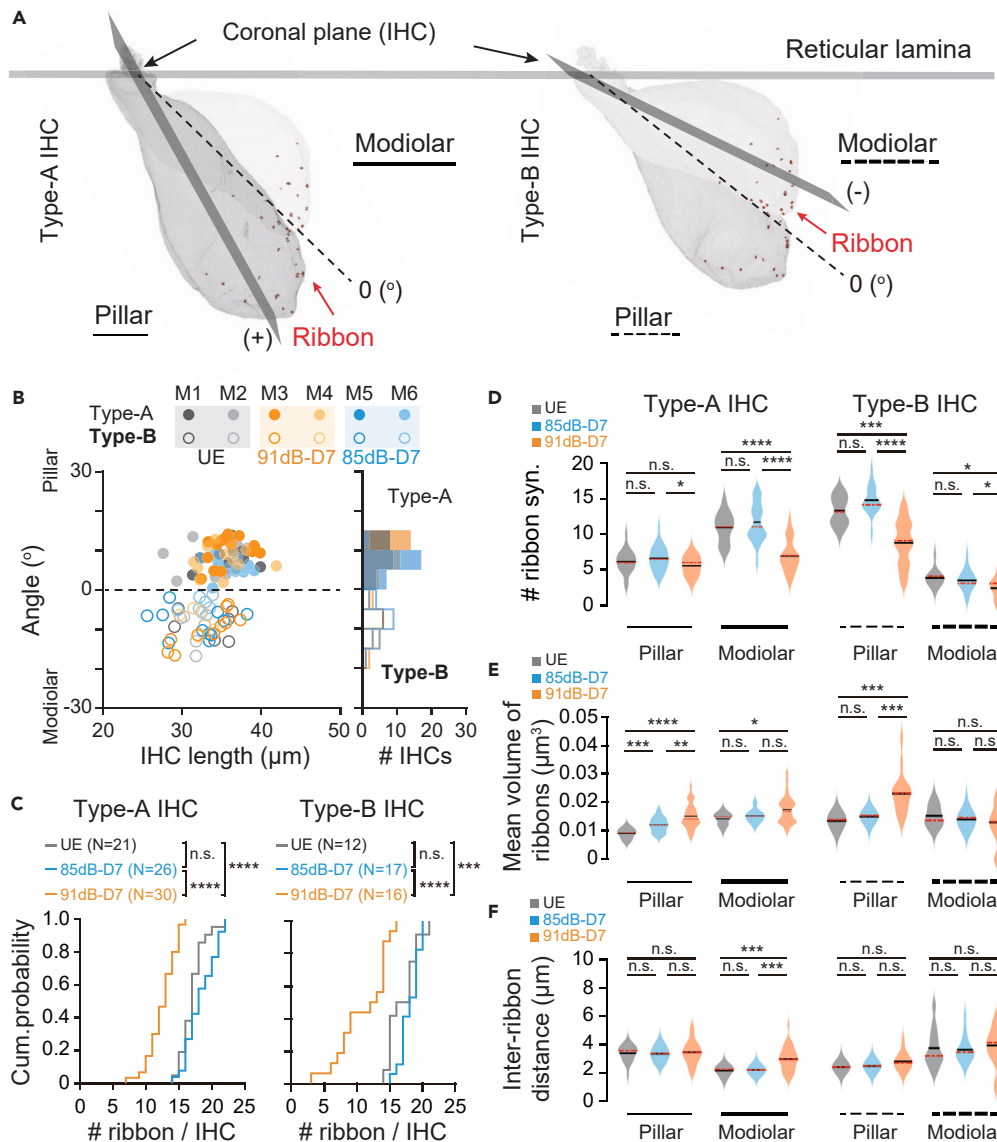


**Figure 3. Distinct spatial patterns of synaptopathy in the IHC subtypes**

(A) Example pairs of the type-A (dark gray) and type-B IHCs (light gray) are shown in sagittal view. They differ from each other by characteristic tilting of the coronal plane, which divides the cell body into the pillar (solid and dashed thin lines) and modiolar hemispheres (solid and dashed thick lines). Red dots at the IHC basolateral surface represent the synaptic ribbons.

(B) Scatterplot of the tilt angles of the IHC coronal plane with respect to the middle plane of IHC pairs (dash line in A). (Right) Bimodal distributed tilt angles can be used to classify type-A IHCs (solid histograms) with positive tilt angles (toward pillars) and type-B IHCs (open histograms) with negative tilt angles (toward modiulus). The average tilt angle is  $8.21^\circ \pm 3.31^\circ$  for the classified 77 type-A IHCs and  $-8.32^\circ \pm 3.90^\circ$  for the 45 type-B IHCs. The type-A IHCs (filled circles,  $35.97 \pm 2.74 \mu\text{m}$ ) have slightly but significantly longer cell bodies than the type-B IHCs (empty circles,  $32.43 \pm 2.83 \mu\text{m}$ ). Two-sample t test:  $p < 0.0001$ . The proportions of type-A IHCs are 63.3% (UE), 61.3% (85dB), and 65.8% (91dB), respectively. One-way ANOVA:  $p = 0.8371$ .

(C) Cumulative probability distribution of ribbon counts from pooled IHC subtypes of the noise-exposed (85dB and 91dB) and unexposed (UE) ears. The median and mean ribbon numbers of the type-A IHCs are 17.0 and  $17.0 \pm 1.8$  (UE,  $N = 21$  IHCs), 18.0 and  $18.3 \pm 2.3$  (85dB,  $N = 26$  IHCs), 13.0 and  $12.5 \pm 2.1$  (91dB,  $N = 30$  IHCs), respectively. Two-sample Kolmogorov-Smirnov tests:  $p = 0.2724$  (UE vs. 85dB),  $p < 0.0001$  (85dB vs. 91dB), and  $p < 0.0001$  (UE vs. 91dB). Right: as to the type-B IHCs, the median and mean ribbon numbers are 17.0 and  $16.9 \pm 2.2$  (UE,  $N = 12$  IHCs), 18.0 and  $18.1 \pm 1.5$  (85dB,  $N = 17$  IHCs), 12.5 and  $11.0 \pm 3.8$  (91dB,  $N = 16$  IHCs), respectively. Two-sample Kolmogorov-Smirnov tests:  $p = 0.1974$  (UE vs. 85dB),  $p < 0.0001$  (85dB vs. 91dB), and  $p = 0.0001$  (UE vs. 91dB).

(D) Left: comparisons of ribbon numbers among the type-A IHCs (solid lines) of the exposed and unexposed ears (UE: gray, 85-dB: blue, 91-dB: orange). The fewest ribbon counts were on the modiolar IHC face in the 91-dB group. There was no significant difference among the pillar ribbons except for a minor decline in the 91-dB group. Right: same comparison for the type-B IHCs (dashed lines). Significantly fewer pillar ribbons are found in the noise-exposed IHCs. Only a minor difference in the modiolar ribbons was observed.

**Figure 3. Continued**

(E) Comparisons of average ribbon volume in the IHCs. As to the type-A IHCs (solid lines), significant ribbon enlargement occurs on the pillar face, whereas no or a minor difference among the modiolar ribbons was noted. As to the type-B IHCs (dashed lines), ribbon size changes are evident on the pillar IHC face, but not on the modiolar face.

(F) Comparisons of inter-ribbon distances as a measure of local ribbon density. As to the type-A IHCs (solid lines), modiolar ribbons are alienated from each other in the 91-dB group, but not on the pillar face. As to the type-B IHCs (dashed lines), ribbon density is maintained in the unexposed and exposed groups. Data in (B) and (C) are presented as mean  $\pm$  SD. Black and red lines represent the mean and the median, respectively. See Table 2 for numbers and statistics in (D), (E), and (F).

upon non-synaptopathic exposure. In the case of 91-dB exposed group, we observed a diminished gradient in the mitochondrial abundance on type-A IHC and fewer mitochondrial-poor terminals onto type-B IHC (Figure 4D).

Next, we focused on the worst-hit areas in terms of synaptopathy and compared the distribution of postsynaptic mitochondrial abundance in the ears on D7 after noise exposure. After the 91-dB exposure, the remaining SGN terminals show enriched mitochondrial content in the region of synaptopathy, namely the modiolar face of type-A IHC (Figure 4E) and the pillar face of type-B IHC (Figure 4F), in comparison with those of the unexposed ear. Such difference between the 91-dB exposed group and the unexposed group can be simulated by a synaptopathy-mimicking exclusion of the top 35% mitochondrion-poor SGN terminals on the modiolar face of type-A IHC (Figure 4E) and the pillar face of type-B IHC (Figure 4F). Unlike the case of synaptopathy, the 85-dB exposed group does not differ from the unexposed group in terms of the SGN mitochondrial counts on either the modiolar face of type-A IHC (Figure 4E inset) or the pillar face of type-B IHC (Figure 4F inset). Further, we noted there is a reduction in the portion of large and complex mitochondria upon synaptopathy (Figures 4G and 4H), implying an activity-dependent mitochondrial plasticity in the survived SGN terminals.

**DISCUSSION**

Mechanosensory hair cells are multi-functionally compartmentalized with specialized organelles, making them attractive model systems for studying the interplay among subcellular components including ribbon synapses, synaptic vesicles, mitochondria, and membrane cisterns.<sup>37–44</sup> With the aid of advanced techniques in serial sectioning, EM reconstruction at whole-cell level has become less labor intensive, contributing to the discoveries of key morphological hallmarks in developing,<sup>5,32</sup> mature,<sup>33,34,45</sup> aging,<sup>46</sup> as well as noise-injured<sup>47</sup> sensory organs.

SBEM is proven capable of visualizing content-rich cytoarchitecture spanning tens of IHCs and OHCs.<sup>33,48</sup> Large EM volume size allows for determining the global orientation difference of the IHCs, identifying outlines of individual cell bodies in densely packed regions, as well as quantifying pre- and postsynaptic structures of the ribbon synapses simultaneously. In addition, it is known that cochlear ultrastructure can vary substantially in a tonotopy-dependent fashion, but determining the precise cochlear location of acquired EM volume has not been established yet, hampering direct inter-study comparison.<sup>5,32,33</sup> Recent work has demonstrated X-ray tomography as a powerful tool for the morphological study of the whole cochlea and its potential to combine with other optical methods.<sup>49,50</sup> In the present work, we demonstrate the practice of targeting a given cochlear tonotopic range by using X-ray-tomographic reconstruction to guide sample trimming and sequential SBEM imaging (Figures 1E, 1F, and S1).

**Synaptopathic and non-synaptopathic acoustic exposure**

Due to the non-linearity of cochlear mechanics, noise damage as well as consequent ribbon loss does not directly relate to the magnitude of ABR threshold elevation (see review<sup>21</sup>). Thus, we calibrated the boundary condition between synaptopathic and non-synaptopathic exposures on the juvenile CBA/CA mice (Figures 1A and 1B). Although the frequency character of noise-induced ABR threshold shifts is consistent with those previously seen on the mature animals, our juvenile mice have acquired ribbon loss already upon a lower noise dose (91 dB, 2h), which has been reported as a non-synaptopathy-inducing condition for the animal at 16 weeks of age.<sup>35</sup> Moreover, complementary to an early study<sup>51</sup> showing accelerated neuronal loss in the young-exposed (4–8 weeks) but not in the old-exposed ( $\geq$  16 weeks) animals to a 100-dB noise exposure, this result corroborates that the juveniles are more vulnerable to acoustic overexposures in terms of not only neuropathy but also synaptopathy. As permissible noise levels for occupational exposure are established in adults,<sup>52,53</sup> it may be advisable to take preventive actions with stricter guidelines for young people.

**Ribbon loss and plasticity in the mature IHCs**

It has been shown that ribbon size is of functional significance and tightly regulated by presynaptic calcium channels.<sup>9,54,55</sup> Emerging volume EM techniques have been employed to dissect the morphological maturation of synaptic ribbons, ranging from late embryonic to adult stages.<sup>5,32,33</sup> In the mature IHCs however, evidence for ribbon maintenance and activity-dependent plasticity remains scarce.<sup>13</sup> Consistent with prior LM observations,<sup>17</sup> post-exposure enlargement of synaptic ribbons was verified by quantitative SBEM (Figures 2C and 2D). More importantly, the enlarged ribbons are not associated with translucent cores (known as “hollow” ribbon, which has been proposed to signify degrading scaffolds), arguing against a long-lasting perturbation of ribbon integrity beyond one week after the noise exposure (Figure S2A). Besides, it is notable that multi-ribbon AZs become more prevalent in the synaptopathic ears (Figures 2D and S2B). The functional property of this structural variant remains to be explored, given that the multi-ribbon AZ is not only retained into adulthood<sup>5,33</sup> but also a hallmark of cochlear aging<sup>56</sup> with a ribbon size increase<sup>57</sup> associated with increased Ca<sup>2+</sup>-dependent exocytotic activity.<sup>58</sup> Finally, the

**Table 2. Ribbon analysis of morphologically subgrouped IHCs**

Number of IHCs	Type-A IHCs		Type-B IHCs	
	21/26/30 (UE/85dB/91dB)		12/17/16 (UE/85dB/91dB)	
Basolateral pole position	Pillar	Modiolar	Pillar	Modiolar
Ribbon synapse counts <sup>a</sup> (UE/85dB/91dB)	6.1 ± 1.6/6.6 ± 1.7/5.6 ± 1.4	10.9 ± 2.2/11.7 ± 2.7/6.9 ± 2.3	13.2 ± 2.1/14.6 ± 2.0/8.7 ± 3.2	3.8 ± 1.2/3.4 ± 1.5/2.3 ± 1.6
Wilcoxon rank-sum test (UE vs. 91dB/UE vs. 85daysB/85dB vs. 91dB)	p = 0.2110/p = 0.4014/p = 0.0285	p < 0.0001/p = 0.3883/p < 0.0001	p = 0.0008/p = 0.1122/ p < 0.0001	p = 0.0130/p = 0.4995/ p = 0.0463
Mean volume of ribbons (μm <sup>3</sup> ) <sup>b</sup> (UE/85dB/91dB)	0.0091 ± 0.0004/0.0121 ± 0.0005/0.0152 ± 0.0008	0.0142 ± 0.0005/0.0152 ± 0.0004/0.0174 ± 0.0009	0.0135 ± 0.0007/0.0151 ± 0.0004/0.0231 ± 0.0018	0.0153 ± 0.0011/0.0141 ± 0.0008/0.0130 ± 0.0021
Wilcoxon rank-sum test (UE vs. 91dB/UE vs. 85daysB/85dB vs. 91dB)	p < 0.0001/p = 0.0002/p = 0.0059	p = 0.0163/p = 0.2895/p = 0.1600	p = 0.0001/p = 0.0968/ p = 0.0001	p = 0.5310/p = 0.4127/ p = 0.8430
Inter-ribbon distance (μm) <sup>b</sup> (UE/85dB/91dB)	3.36 ± 0.13/3.32 ± 0.11/3.44 ± 0.15	2.16 ± 0.08/2.22 ± 0.06/2.98 ± 0.16	2.41 ± 0.08/2.48 ± 0.08/2.80 ± 0.18	3.72 ± 0.38/3.62 ± 0.24/3.89 ± 0.37
Wilcoxon rank-sum test (UE vs. 91dB/UE vs. 85daysB/85dB vs. 91dB)	p = 0.9470/p = 0.5279/ p = 0.6400	p = 0.0004/p = 0.6922/ p = 0.0004	p = 0.0794/p = 0.6430/ p = 0.1320	p = 0.4060/p = 0.9417/ p = 0.2540

<sup>a</sup>Data are represented as mean ± SD.

<sup>b</sup>Data are represented as mean ± SEM.

appearance of enlarged and multi-ribbons leads to an increased ribbon size heterogeneity (Figure 2D), implying that the IHC coding deficit might not be a simple consequence of the selective loss of high-threshold SGN fibers (preferentially on the modiolar IHC face and postsynaptic to large ribbons) as extensively debated in the field (see reviews<sup>20,21</sup>), but possibly involve maladaptive changes in both pre- and postsynaptic structures.

### Distinct spatial patterns of synaptopathy in the mouse IHCs

In the mouse mid-cochlear region, staggered IHCs with alternating basolateral pole positions are prevalent.<sup>30</sup> Considering that the postsynaptic SGNs with molecular diversity are arranged with complementary spatial preferences<sup>10–12,59</sup>, these two morphological subtypes of IHCs may favor distinct SGN compositions. In this way, adjacent IHCs with different receptive fields can encode over a broad audible range. In line with this notion, our recent study showed that staggered IHCs are not only morphologically distinct but also differ in their ribbon size and density gradient.<sup>31</sup> But note that the IHC staggering has only been convincingly shown in mice of different strains<sup>30–32</sup> and probably also in cat. Whether it is a shared structural feature of the most sensitive mid-cochlea among mammals requires future investigation.

Single fiber recordings in guinea pigs suggested that the low-SR SGN fibers - predominantly facing large modiolar ribbons - are more vulnerable to noise insult,<sup>22</sup> but also see more recent work with alternative interpretation.<sup>60</sup> In line with this notion, preferential ribbon loss on the modiolar IHC face was observed in the recovered ears of CBA/CaJ mice on D7 post a 2-hour synaptopathic exposure.<sup>17</sup> Our results suggest that the worst-hit areas of noise damage are the IHC subregions with high ribbon density, namely the modiolar face of type-A as well as the pillar face of type-B IHCs (Figure 3D). In addition to cropping image stacks that only contain well-aligned IHCs,<sup>61</sup> different ways of quantification for LM and SBEM may explain this discrepancy. In the LM studies,<sup>17,30,62</sup> a global modiolar-pillar axis is routinely used and thereby the type-A IHC contributes more to the LM-classified "pillar" ribbons while the type-B IHC to the "modiolar" ribbons. Indeed, we find there is more severe ribbon loss in the exposed type-B IHC (Figure 3C), matching the proposed modiolar preference. But in fact, the type-B IHC loses more ribbons on the pillar face as uncovered by our SBEM quantification (Figure 3D).

At the presynaptic side, the mixed spatial patterns of synaptopathy, accompanied by substantial ribbon volume changes, may reflect some sort of adaptation and reorganization. It is tempting to speculate that mature ribbon synapse also undergoes activity-dependent plasticity,<sup>13</sup> presumably under tight regulation of local interplay between presynaptic- and mitochondrial-Ca<sup>2+</sup> influx, as shown recently in the zebrafish lateral-line hair cells.<sup>63,64</sup> If so, there might be an underdetermined role of proper presynaptic organization, for instance, the mitochondrial and membrane networks,<sup>31,34,65</sup> in shaping the spatial gradient of IHC ribbons to match preferred postsynaptic SGN targets for a normal hearing function. In turn, noise-induced presynaptic disorganization, as reported recently,<sup>47</sup> may lead to limited recovery and maladaptation with respect to the synaptic ribbon diversification and thereby an impaired level encoding of sounds.

### Postsynaptic mitochondrial content of the ribbon synapse

At the postsynaptic side, it is a common belief that the paucity of terminal mitochondria causes heightened vulnerability of those SGN fibers postsynaptic to the modiolar ribbons by glutamate-mediated calcium overload.<sup>21</sup> Here, our result provides critical pieces of

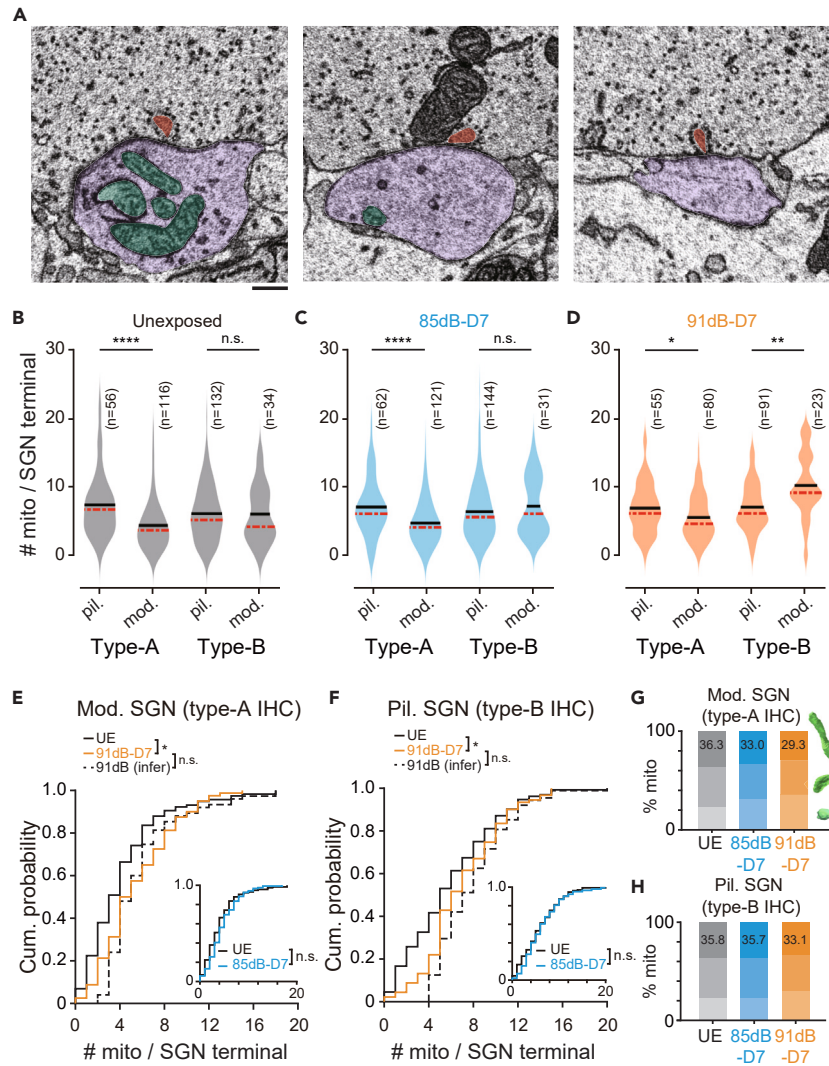


**Figure 4. Postsynaptic mitochondrial content in the SGN terminal**

(A) Representative EM images of different mitochondrial content (green) in the SGN terminal (purple) postsynaptic to a confirmed ribbon (red). Scale bar, 1  $\mu$ m.

(B) Spatial gradient of terminal mitochondrion number in the unexposed ears (gray). In the type-A IHCs, mitochondrion-rich SGN terminals are preferentially enriched on the pillar face ( $7.2 \pm 4.6$  [pil.] vs.  $4.2 \pm 3.6$  [mod.], Wilcoxon rank-sum test:  $p < 0.0001$ ). As to the type-B IHCs, mitochondrion-rich SGN terminals are prevalent on both IHC faces ( $5.9 \pm 4.0$  [pil.] vs.  $5.9 \pm 4.1$  [mod.], Wilcoxon rank-sum test:  $p = 0.8598$ ).

(C) Same as (B), but for the 85-dB exposed group (blue). For the type-A IHCs:  $7.0 \pm 4.1$  (pil.) vs.  $4.6 \pm 3.1$  (mod.). Wilcoxon rank-sum test:  $p < 0.0001$ . For the type-B IHCs:  $6.3 \pm 4.2$  (pil.) vs.  $7.1 \pm 4.2$  (mod.). Wilcoxon rank-sum test:  $p = 0.3483$ .

(D) Same as (B), but for the 91-dB exposed group (orange). For the type-A IHCs:  $6.8 \pm 3.7$ , (pil.) vs.  $5.4 \pm 3.3$ , (mod.), Wilcoxon rank-sum test,  $p = 0.0321$ . For the type-B IHCs:  $6.9 \pm 3.4$  (pil.) vs.  $10.0 \pm 4.7$  (mod.). Wilcoxon rank-sum test:  $p = 0.0019$ .

(E) Cumulative probability distribution of mitochondrion number in the SGN terminals contacting the modiolar face of type-A IHCs. The median and mean mitochondrial numbers are 3.0 and  $4.2 \pm 3.6$  ( $n = 116$ ) for the unexposed group (black line), 4.5 and  $5.4 \pm 3.3$  ( $n = 80$ ) for the 91-dB exposed group (orange line), as well as 5.0 and  $5.8 \pm 3.5$  ( $n = 75$ ) for the artificial synaptotrophic group which is inferred by excluding 36% SGNs with the fewest mitochondria (black dashed line). Inset: same distribution between the unexposed (black line) and the 85-dB exposed ears (blue line, 4.0 and  $4.6 \pm 3.1$ ,  $n = 121$ ). Two-sample Kolmogorov-Smirnov tests:  $p = 0.0453$  (UE vs. 91dB),  $p = 0.1801$  (91dB vs. 91dB-inferred),  $p = 0.3106$  (UE vs. 85dB).

(F) Same as in (E), but for the pillar SGN terminals of type-B IHCs. The median and mean mitochondrial numbers are 5.0 and  $5.9 \pm 4.0$  (UE,  $n = 132$ ), 6.0 and  $6.9 \pm 3.4$  (91dB,  $n = 91$ ), 7.0 and  $7.9 \pm 3.2$  (91dB-inferred, excluded the top 34% mitochondria-poor SGNs,  $n = 88$ ), 6.0 and  $6.3 \pm 4.2$  (inset: 85dB,  $n = 144$ ), respectively. Two-sample Kolmogorov-Smirnov tests:  $p = 0.0263$  (UE vs. 91dB),  $p = 0.3811$  (91dB vs. 91dB-inferred), and  $p = 0.4157$  (UE vs. 85dB).

(G) The percentage of terminal mitochondria of different sizes. Comparison of SGNs contacting the modiolar face of type-A IHCs among the unexposed (UE) and exposed groups (85dB and 91dB). Three classes of terminal mitochondria are shown (green): round (below), oval (middle), as well as large and complex (top). 36.3% (UE), 33.0% (85dB), and 29.3% (91dB) of the total population are composed of large and complex mitochondria.

(H) Same as (G), but for the pillar SGNs on the type-B IHCs. The percentages of large and complex mitochondria are 35.8% (UE), 35.7% (85dB), and 33.1% (91dB) in the SGN terminals, respectively. Black and red lines represent the mean and the median in (B), (C), and (D). Data in (B-F) are presented as mean  $\pm$  SD.

experimental evidence from the mouse that is more widely used in anatomical studies of synapses at the light microscopic level. Unlike the extreme scenario in the cat cochlea, we found that mitochondrion-rich and -poor SGN terminals of mice are not spatially segregated along the global modiolar-pillar axis of the organ of Corti as well as in the type-B IHCs (Figure 4B). Nonetheless, the remaining SGN terminals of the synaptopathic ears appear an enriched mitochondrial content, matching the inference based on survivorship bias (Figures 4E and 4F). Mitochondrion-poor terminals tend to show up at the intermediate zone between two staggered IHCs (Figures 4B–4D), where local high synapse density is evident (Figure 3D). This leads us to speculate that overcrowded postsynaptic space may favor the loss of small-sized SGN terminals with limited mitochondrial content. Moreover, we do capture a considerable fraction of big and mitochondrion-rich SGN terminals in those regions and facing large presynaptic ribbons, suggesting that opposing volume gradients of presynaptic ribbons and postsynaptic SGN terminals may be vague in the mid-cochlea of CBA/Ca mouse. This has been recently quantified using immunofluorescence of CTBP2 and GluA2 and confocal microscopy in different mouse stains.<sup>66</sup> Nevertheless, it remains elusive for future investigations how this uneven ribbon synapse distribution along the IHC basolateral pole and heterogeneous mitochondrial content in putative low- and high-SR SGN fibers are modulated by the transcriptomic changes in response to sensory experience including acoustic trauma.<sup>67,68</sup>

### Limitations of the study

We show distinct synaptopathy patterns in morphological subtypes of mouse mid-cochlear IHCs after the noise exposure. The comparisons, however, were made only on post-exposure D7 between synaptopathic, non-synaptopathic, and unexposed ears of CBA/Ca male mice. Subsequent work will include both male and female mice of different strains to evaluate possible gender- and strain-specific differences. Moreover, it will be highly interesting to study the activity-induced pre- and postsynaptic ultrastructural changes during the early stage of noise insult in a temporally resolved manner. These mechanistic insights will be essential for understanding the physiology and pathology of synaptic remodeling in our organ of hearing.

### STAR★METHODS

Detailed methods are provided in the online version of this paper and include the following:

- KEY RESOURCES TABLE
- RESOURCE AVAILABILITY
  - Lead contact
  - Materials availability
  - Data and code availability
- EXPERIMENTAL MODEL AND STUDY PARTICIPANT DETAILS
  - Animals
- METHOD DETAILS
  - Acoustic overexposure
  - Auditory brainstem responses (ABRs)
  - Sample preparation
  - X-ray microscopy (XRM) and serial block-face EM (SBEM)
  - Reconstruction of IHC and ribbon synapse
  - Determination of IHC coronal plane and tilt angle
  - Measurement of ribbon and mitochondrion
- QUANTIFICATION AND STATISTICAL ANALYSIS

### SUPPLEMENTAL INFORMATION

Supplemental information can be found online at <https://doi.org/10.1016/j.isci.2024.108825>.

### ACKNOWLEDGMENTS

We thank Prof. Zhiwu Huang for the help with the noise exposure experiment. We thank Xu Ding for the help in the early stages of this work. We thank Dr. Yanhua Zhu (Shanghai Jiao Tong University Instrumental Analysis Center) for the assistance of XRM imaging. This work was supported by the National Natural Science Foundation of China (82171133 to Y.H., 32171461 to H.H.), Industrial Support Fund of Huangpu District in Shanghai (XK2019011 to Y.H.), Innovative Research Team of High-level Local Universities in Shanghai (SHSMU-ZLCX20211700), the Shanghai Key Laboratory of Translational Medicine on Ear and Nose Diseases (14DZ2260300).

### AUTHOR CONTRIBUTIONS

Y.H. designed and supervised the study; Y.L. and B.L. carried out the animal experiments, Y.L., J.L., H.W., and S.W. analyzed the data; J.L. and H.H. contributed to the segmentation and 3D reconstruction; F.W. assisted with the EM acquisition; Y.H., Y.L., H.W., and J.L. drafted the manuscript. All authors commented on the manuscript.

## DECLARATION OF INTERESTS

The authors declare no competing financial interests.

Received: July 6, 2023

Revised: October 16, 2023

Accepted: January 3, 2024

Published: January 8, 2024

## REFERENCES

- Fettiplace, R. (2017). Hair Cell Transduction, Tuning, and Synaptic Transmission in the Mammalian Cochlea. *Compr. Physiol.* 7, 1197–1227.
- Huet, A., Batrel, C., Wang, J., Desmadryl, G., Nouvian, R., Puel, J.L., and Bourien, J. (2019). Sound Coding in the Auditory Nerve: From Single Fiber Activity to Cochlear Mass Potentials in Gerbils. *Neuroscience* 407, 83–92.
- Moser, T., Grabner, C.P., and Schmitz, F. (2020). Sensory Processing at Ribbon Synapses in the Retina and the Cochlea. *Physiol. Rev.* 100, 103–144.
- Shrestha, B.R., and Goodrich, L.V. (2019). Wiring the Cochlea for Sound Perception. In *The Oxford Handbook of the Auditory Brainstem*, K. Kandler, ed. (Oxford University Press).
- Michanski, S., Smaluch, K., Steyer, A.M., Chakrabarti, R., Setz, C., Oestreicher, D., Fischer, C., Möbius, W., Moser, T., Vogl, C., and Wichmann, C. (2019). Mapping developmental maturation of inner hair cell ribbon synapses in the apical mouse cochlea. *Proc. Natl. Acad. Sci. USA* 116, 6415–6424.
- Joselevitch, C., and Zenisek, D. (2020). Direct Observation of Vesicle Transport on the Synaptic Ribbon Provides Evidence That Vesicles Are Mobilized and Prepared Rapidly for Release. *J. Neurosci.* 40, 7390–7404.
- Vaithianathan, T., Henry, D., Akmentin, W., and Matthews, G. (2016). Nanoscale dynamics of synaptic vesicle trafficking and fusion at the presynaptic active zone. *Elife* 5, e13245.
- Neef, J., Urban, N.T., Ohn, T.L., Frank, T., Jean, P., Hell, S.W., Willig, K.I., and Moser, T. (2018). Quantitative optical nanophysiology of Ca(2+) signaling at inner hair cell active zones. *Nat. Commun.* 9, 290.
- Özçete, Ö.D., and Moser, T. (2021). A sensory cell diversifies its output by varying Ca(2+) influx-release coupling among active zones. *EMBO J.* 40, e106010.
- Shrestha, B.R., Chia, C., Wu, L., Kujawa, S.G., Liberman, M.C., and Goodrich, L.V. (2018). Sensory Neuron Diversity in the Inner Ear Is Shaped by Activity. *Cell* 174, 1229–1246.e17.
- Petitpré, C., Wu, H., Sharma, A., Tokarska, A., Fontanet, P., Wang, Y., Helmbacher, F., Yackle, K., Silberberg, G., Hadjab, S., and Lallemand, F. (2018). Neuronal heterogeneity and stereotyped connectivity in the auditory afferent system. *Nat. Commun.* 9, 3691.
- Sun, S., Babola, T., Pregelornig, G., So, K.S., Nguyen, M., Su, S.S.M., Palermo, A.T., Bergles, D.E., Burns, J.C., and Müller, U. (2018). Hair Cell Mechanotransduction Regulates Spontaneous Activity and Spiral Ganglion Subtype Specification in the Auditory System. *Cell* 174, 1247–1263.e15.
- Voon, R.A., and Vogl, C. (2020). Molecular Assembly and Structural Plasticity of Sensory Ribbon Synapses—A Presynaptic Perspective. *Int. J. Mol. Sci.* 21, 8758.
- Sun, S., Siebald, C., and Müller, U. (2021). Subtype maturation of spiral ganglion neurons. *Curr. Opin. Otolaryngol. Head Neck Surg.* 29, 391–399.
- Moser, T., Karagulyan, N., Neef, J., and Jaime Tobón, L.M. (2023). Diversity matters - extending sound intensity coding by inner hair cells via heterogeneous synapses. *EMBO J.* 42, e114587.
- Kujawa, S.G., and Liberman, M.C. (2009). Adding insult to injury: cochlear nerve degeneration after "temporary" noise-induced hearing loss. *J. Neurosci.* 29, 14077–14085.
- Liberman, L.D., Suzuki, J., and Liberman, M.C. (2015). Dynamics of cochlear synaptopathy after acoustic overexposure. *J. Assoc. Res. Otolaryngol.* 16, 205–219.
- Kujawa, S.G., and Liberman, M.C. (2015). Synaptopathy in the noise-exposed and aging cochlea: Primary neural degeneration in acquired sensorineural hearing loss. *Hear. Res.* 330, 191–199.
- Shi, L., Chang, Y., Li, X., Aiken, S.J., Liu, L., and Wang, J. (2016). Coding Deficits in Noise-Induced Hidden Hearing Loss May Stem from Incomplete Repair of Ribbon Synapses in the Cochlea. *Front. Neurosci.* 10, 231.
- Chen, H., Shi, L., Liu, L., Yin, S., Aiken, S., and Wang, J. (2019). Noise-induced Cochlear Synaptopathy and Signal Processing Disorders. *Neuroscience* 407, 41–52.
- Liberman, M.C. (2017). Noise-induced and age-related hearing loss: new perspectives and potential therapies. *F1000Res.* 6, 927.
- Furman, A.C., Kujawa, S.G., and Liberman, M.C. (2013). Noise-induced cochlear neuropathy is selective for fibers with low spontaneous rates. *J. Neurophysiol.* 110, 577–586.
- Hu, N., Rutherford, M.A., and Green, S.H. (2020). Protection of cochlear synapses from noise-induced excitotoxic trauma by blockade of Ca(2+)-permeable AMPA receptors. *Proc. Natl. Acad. Sci. USA* 117, 3828–3838.
- Kim, K.X., Payne, S., Yang-Hood, A., Li, S.Z., Davis, B., Carlquist, J., V-Ghaffari, B., Gantz, J.A., Kallojgeri, D., Fitzpatrick, J.A.J., et al. (2019). Vesicular Glutamatergic Transmission in Noise-Induced Loss and Repair of Cochlear Ribbon Synapses. *J. Neurosci.* 39, 4434–4447.
- Puel, J.L., Ruel, J., Gervais d'Aldin, C., and Pujol, R. (1998). Excitotoxicity and repair of cochlear synapses after noise-trauma induced hearing loss. *Neuroreport* 9, 2109–2114.
- Hakuba, N., Koga, K., Gyo, K., Usami, S.I., and Tanaka, K. (2000). Exacerbation of noise-induced hearing loss in mice lacking the glutamate transporter GLAST. *J. Neurosci.* 20, 8750–8753.
- Liberman, M.C. (1980). Morphological differences among radial afferent fibers in the cat cochlea: an electron-microscopic study of serial sections. *Hear. Res.* 3, 45–63.
- Liberman, M.C. (1982). Single-neuron labeling in the cat auditory nerve. *Science* 216, 1239–1241.
- Suthakar, K., and Liberman, M.C. (2021). Auditory-nerve responses in mice with noise-induced cochlear synaptopathy. *J. Neurophysiol.* 126, 2027–2038.
- Yin, Y., Liberman, L.D., Maison, S.F., and Liberman, M.C. (2014). Olivocochlear innervation maintains the normal modiolar-pillar and habenular-cuticular gradients in cochlear synaptic morphology. *J. Assoc. Res. Otolaryngol.* 15, 571–583.
- Liu, J., Wang, S., Lu, Y., Wang, H., Wang, F., Qiu, M., Xie, Q., Han, H., and Hua, Y. (2022). Aligned Organization of Synapses and Mitochondria in Auditory Hair Cells. *Neurosci. Bull.* 38, 235–248.
- Payne, S.A., Joens, M.S., Chung, H., Skigen, N., Frank, A., Gattani, S., Vaughn, K., Schwed, A., Nester, M., Bhattacharya, A., et al. (2021). Maturation of Heterogeneity in Afferent Synapse Ultrastructure in the Mouse Cochlea. *Front. Synaptic Neurosci.* 13, 678575.
- Hua, Y., Ding, X., Wang, H., Wang, F., Lu, Y., Neef, J., Gao, Y., Moser, T., and Wu, H. (2021). Electron Microscopic Reconstruction of Neural Circuitry in the Cochlea. *Cell Rep.* 34, 108551.
- Bullen, A., West, T., Moores, C., Ashmore, J., Fleck, R.A., MacLellan-Gibson, K., and Forge, A. (2015). Association of intracellular and synaptic organization in cochlear inner hair cells revealed by 3D electron microscopy. *J. Cell Sci.* 128, 2529–2540.
- Fernandez, K.A., Jeffers, P.W.C., Lall, K., Liberman, M.C., and Kujawa, S.G. (2015). Aging after noise exposure: acceleration of cochlear synaptopathy in "recovered" ears. *J. Neurosci.* 35, 7509–7520.
- Grierson, K.E., Hickman, T.T., and Liberman, M.C. (2022). Dopaminergic and cholinergic innervation in the mouse cochlea after noise-induced or age-related synaptopathy. *Hear. Res.* 422, 108533.
- Spicer, S.S., Thomopoulos, G.N., and Schulte, B.A. (1999). Novel membranous structures in apical and basal compartments of inner hair cells. *J. Comp. Neurol.* 409, 424–437.
- Spicer, S.S., Qu, C., Smythe, N., and Schulte, B.A. (2007). Mitochondria-activated cisternae generate the cell specific vesicles in auditory hair cells. *Hear. Res.* 233, 40–45.
- Lioudyno, M., Hiel, H., Kong, J.H., Katz, E., Waldman, E., Parameshwaran-Iyer, S., Glowatzki, E., and Fuchs, P.A. (2004). A "synaptoplasmic cistern" mediates rapid inhibition of cochlear hair cells. *J. Neurosci.* 24, 11160–11164.

40. Lysakowski, A., and Goldberg, J.M. (1997). A regional ultrastructural analysis of the cellular and synaptic architecture in the chinchilla cristae ampullares. *J. Comp. Neurol.* **389**, 419–443.
41. Esterberg, R., Hailey, D.W., Rubel, E.W., and Raible, D.W. (2014). ER-mitochondrial calcium flow underlies vulnerability of mechanosensory hair cells to damage. *J. Neurosci.* **34**, 9703–9719.
42. Hashimoto, S., Kimura, R.S., and Takasaka, T. (1990). Computer-aided three-dimensional reconstruction of the inner hair cells and their nerve endings in the guinea pig cochlea. *Acta Otolaryngol.* **109**, 228–234.
43. Kantardzhieva, A., Liberman, M.C., and Sewell, W.F. (2013). Quantitative analysis of ribbons, vesicles, and cisterns at the cat inner hair cell synapse: correlations with spontaneous rate. *J. Comp. Neurol.* **521**, 3260–3271.
44. Chakrabarti, R., Michanski, S., and Wichmann, C. (2018). Vesicle sub-pool organization at inner hair cell ribbon synapses. *EMBO Rep.* **19**, e44937.
45. Dow, E., Siletti, K., and Hudspeth, A.J. (2015). Cellular projections from sensory hair cells form polarity-specific scaffolds during synaptogenesis. *Genes Dev.* **29**, 1087–1094.
46. Lauer, A.M., Fuchs, P.A., Ryugo, D.K., and Francis, H.W. (2012). Efferent synapses return to inner hair cells in the aging cochlea. *Neurobiol. Aging* **33**, 2892–2902.
47. Bullen, A., Anderson, L., Bakay, W., and Forge, A. (2019). Localized disorganization of the cochlear inner hair cell synaptic region after noise exposure. *Biol. Open* **8**, bio038547.
48. Wang, H., Wang, S., Lu, Y., Chen, Y., Huang, W., Qiu, M., Wu, H., and Hua, Y. (2021). Cytoarchitecture and Innervation of the Mouse Cochlear Amplifier Revealed by Large-scale Volume Electron Microscopy. *J. Comp. Neurol.* **529**, 2958–2969.
49. Keppeler, D., Kampshoff, C.A., Thirumalai, A., Duque-Afonso, C.J., Schaeper, J.J., Quilitz, T., Töpperwien, M., Vogl, C., Hessler, R., Meyer, A., et al. (2021). Multiscale photonic imaging of the native and implanted cochlea. *Proc. Natl. Acad. Sci. USA* **118**, e2014472118.
50. Lu, Y., Wang, F., Wang, H., Bastians, P., and Hua, Y. (2021). Large-scale 3D imaging of mouse cochlea using serial block-face scanning electron microscopy. *STAR Protoc.* **2**, 100515.
51. Kujawa, S.G., and Liberman, M.C. (2006). Acceleration of age-related hearing loss by early noise exposure: evidence of a misspent youth. *J. Neurosci.* **26**, 2115–2123.
52. Daniell, W.E., Swan, S.S., McDaniel, M.M., Camp, J.E., Cohen, M.A., and Stebbins, J.G. (2006). Noise exposure and hearing loss prevention programmes after 20 years of regulations in the United States. *Occup. Environ. Med.* **63**, 343–351.
53. Davis, R.R., and Clavier, O. (2017). Impulsive noise: A brief review. *Hear. Res.* **349**, 34–36.
54. Frank, T., Khimich, D., Neef, A., and Moser, T. (2009). Mechanisms contributing to synaptic Ca<sup>2+</sup> signals and their heterogeneity in hair cells. *Proc. Natl. Acad. Sci. USA* **106**, 4483–4488.
55. Sheets, L., Kindt, K.S., and Nicolson, T. (2012). Presynaptic CaV1.3 channels regulate synaptic ribbon size and are required for synaptic maintenance in sensory hair cells. *J. Neurosci.* **32**, 17273–17286.
56. Stamatakis, S., Francis, H.W., Lehar, M., May, B.J., and Ryugo, D.K. (2006). Synaptic alterations at inner hair cells precede spiral ganglion cell loss in aging C57BL/6J mice. *Hear. Res.* **221**, 104–118.
57. Jeng, J.Y., Ceriani, F., Olt, J., Brown, S.D.M., Holley, M.C., Bowl, M.R., Johnson, S.L., and Marcotti, W. (2020). Pathophysiological changes in inner hair cell ribbon synapses in the ageing mammalian cochlea. *J. Physiol.* **598**, 4339–4355.
58. Peineau, T., Belleudy, S., Pietropaolo, S., Bouleau, Y., and Dulon, D. (2021). Synaptic Release Potentiation at Aging Auditory Ribbon Synapses. *Front. Aging Neurosci.* **13**, 756449.
59. Sherrill, H.E., Jean, P., Driver, E.C., Sanders, T.R., Fitzgerald, T.S., Moser, T., and Kelley, M.W. (2019). Pou4f1 Defines a Subgroup of Type I Spiral Ganglion Neurons and Is Necessary for Normal Inner Hair Cell Presynaptic Ca(2+) Signaling. *J. Neurosci.* **39**, 5284–5298.
60. Hickman, T.T., Hashimoto, K., Liberman, L.D., and Liberman, M.C. (2021). Cochlear Synaptic Degeneration and Regeneration After Noise: Effects of Age and Neuronal Subgroup. *Front. Cell. Neurosci.* **15**, 684706.
61. Liberman, L.D., Wang, H., and Liberman, M.C. (2011). Opposing gradients of ribbon size and AMPA receptor expression underlie sensitivity differences among cochlear-nerve/hair-cell synapses. *J. Neurosci.* **31**, 801–808.
62. Hickman, T.T., Hashimoto, K., Liberman, L.D., and Liberman, M.C. (2020). Synaptic migration and reorganization after noise exposure suggests regeneration in a mature mammalian cochlea. *Sci. Rep.* **10**, 19945.
63. Wong, H.T.C., Zhang, Q., Beirl, A.J., Petralia, R.S., Wang, Y.X., and Kindt, K. (2019). Synaptic mitochondria regulate hair-cell synapse size and function. *Elife* **8**, e48914.
64. Lukasz, D., Beirl, A., and Kindt, K. (2022). Chronic neurotransmission increases the susceptibility of lateral-line hair cells to ototoxic insults. *Elife* **11**, e77775.
65. McQuate, A., Knecht, S., and Raible, D.W. (2023). Activity regulates a cell type-specific mitochondrial phenotype in zebrafish lateral line hair cells. *Elife* **12**, e80468.
66. Reijntjes, D.O.J., Köppl, C., and Pyott, S.J. (2020). Volume gradients in inner hair cell-auditory nerve fiber pre- and postsynaptic proteins differ across mouse strains. *Hear. Res.* **390**, 107933.
67. Milon, B., Shulman, E.D., So, K.S., Cederroth, C.R., Lipford, E.L., Sperber, M., Sellon, J.B., Sarlus, H., Pregernig, G., Shuster, B., et al. (2021). A cell-type-specific atlas of the inner ear transcriptional response to acoustic trauma. *Cell Rep.* **36**, 109758.
68. Frank, M.M., Sitko, A.A., Suthakar, K., Torres Cadenas, L., Hunt, M., Yuk, M.C., Weisz, C.J.C., and Goodrich, L.V. (2023). Experience-dependent flexibility in a molecularly diverse central-to-peripheral auditory feedback system. *Elife* **12**, e83855.
69. Boergens, K.M., Berning, M., Bocklisch, T., Bräunlein, D., Drawitsch, F., Frohnhofen, J., Herold, T., Otto, P., Rzepka, N., Werkmeister, T., et al. (2017). webKnossos: efficient online 3D data annotation for connectomics. *Nat. Methods* **14**, 691–694.
70. Wang, H., Li, B., Lu, Y., Han, K., Sheng, H., Zhou, J., Qi, Y., Wang, X., Huang, Z., Song, L., and Hua, Y. (2021). Real-time threshold determination of auditory brainstem responses by cross-correlation analysis. *iScience* **24**, 103285.
71. Zhang, Y., Lin, G., Wang, Y., Xue, N., Lin, X., Du, T., Xiong, W., and Song, L. (2022). Prestin derived OHC surface area reduction underlies age-related rescaling of frequency place coding. *Hear. Res.* **423**, 108406.
72. Müller, M., von Hünenbein, K., Hoidis, S., and Smolders, J.W.T. (2005). A physiological place-frequency map of the cochlea in the CBA/J mouse. *Hear. Res.* **202**, 63–73.

## STAR★METHODS

## KEY RESOURCES TABLE

REAGENT or RESOURCE	SOURCE	IDENTIFIER
<b>Deposited data</b>		
SBEM raw dataset (M1)	This paper	<a href="https://wklink.org/3892">https://wklink.org/3892</a>
SBEM raw dataset (M2)	This paper	<a href="https://wklink.org/7172">https://wklink.org/7172</a>
SBEM raw dataset (M3)	This paper	<a href="https://wklink.org/1329">https://wklink.org/1329</a>
SBEM raw dataset (M4)	This paper	<a href="https://wklink.org/9122">https://wklink.org/9122</a>
SBEM raw dataset (M5)	This paper	<a href="https://wklink.org/7842">https://wklink.org/7842</a>
SBEM raw dataset (M6)	This paper	<a href="https://wklink.org/1728">https://wklink.org/1728</a>
Annotations and codes used for analysis	This paper	<a href="http://www.shipm.cn/jyz_web/html/DefaultSite/jyz_syxz_hyf_kycg/List/index.htm">http://www.shipm.cn/jyz_web/html/DefaultSite/jyz_syxz_hyf_kycg/List/index.htm</a>
<b>Experimental models: Organisms/strains</b>		
Mouse: CBA/Ca	Sino-British SIPPR/BK Lab. Animal Ltd (Shanghai, China)	CBA/Ca/Bkl
<b>Software and algorithms</b>		
Code used for the IHC segmentation	This paper	<a href="https://github.com/MiRA-lab-dev/IHC_organelles_detection">https://github.com/MiRA-lab-dev/IHC_organelles_detection</a>
BioSigRZ	Tucker-Davis Tech. Inc	version 5.7.6
SigGen RP	Tucker-Davis Tech. Inc	version 5.7.6
webKNOSSOS	Boergens et al. <sup>69</sup>	<a href="https://webknossos.org">https://webknossos.org</a>
Amira	Thermo Scientific, Inc	release 2019
MATLAB and Statistics Toolbox	MathWorks, Inc	release 2021a
<b>Other</b>		
Loudspeaker	HiVi Acoustic, Inc.	X4
Sound card	TASCAM, Inc.	US-366
Acoustimeter	Hangzhou Aihua Instruments Co., Ltd.	AWA6228+
RZ6 Processor	Tucker-Davis Tech. Inc	N/A
Speaker	Tucker-Davis Tech. Inc	MF1
Abdomen	Harvard Apparatus, Inc.	Homeothermic Monitoring System

## RESOURCE AVAILABILITY

## Lead contact

Further information and requests for resources and reagents should be directed to and will be fulfilled by the Lead Contact, Y.H. ([yunfeng.hua@shsmu.edu.cn](mailto:yunfeng.hua@shsmu.edu.cn)).

## Materials availability

This study did not generate new unique reagents.

## Data and code availability

- The raw microscopy image data supporting the current study can be browsed at links (<https://wklink.org/3892>, <https://wklink.org/7172>, <https://wklink.org/1329>, <https://wklink.org/9122>, <https://wklink.org/7842>, <https://wklink.org/1728>) and are available from the corresponding author on request. All annotations are publicly available via links listed in the [key resources table](#).
- All original code is publicly available as of the date of publication ([https://github.com/MiRA-lab-dev/IHC\\_organelles\\_detection](https://github.com/MiRA-lab-dev/IHC_organelles_detection)).
- Any additional information required to reanalyze the data reported in this paper is available from the [lead contact](#) upon request.

## EXPERIMENTAL MODEL AND STUDY PARTICIPANT DETAILS

### Animals

CBA/Ca mice (male, postnatal day 28) were purchased from Shanghai Jihui Experimental Animal Feeding Co., Ltd. (Shanghai, China). During the experiment (except for the noise exposure), animals were raised in the same acoustic environment and sacrificed at the same age (postnatal day 42). Experiments were conducted at the Ear Institute of Shanghai Jiao Tong University School of Medicine and Shanghai Institute of Precision Medicine. All procedures were approved by the Institutional Authority for Laboratory Animal Care of Shanghai Ninth People's Hospital (SH9H-2020-A65-1).

## METHOD DETAILS

### Acoustic overexposure

The acoustic overexposure was carried out in a sound-attenuating chamber (Shanghai Shino Acoustic Equipment Co. Ltd, China). Two acoustic overstimulation protocols were used in this study: an octave-band of noise (8-16 kHz) at 91 or 85 dB for 2 hours (Figure 1B). During the noise exposure, awake animals were kept without restraint in 18 x 18 x 10 cm<sup>3</sup> sized cells (1 animal/cell) in a subdivided cage by barbed wires. The cage was placed directly below the horn of the loudspeaker (X4, HiVi Acoustic, Inc.) connected to a sound card (US-366, TASCAM, Inc.). The octave-band waveform was custom-made (a gift from Prof. Bo Zhong, National Institute of Metrology, China) and real-time monitored by Adobe Audition Software. Before each exposure session, the noise was calibrated to the target sound pressure level using an acoustimeter (AWA6228+, Hangzhou Aihua Instruments Co., Ltd., China) placed in the cage.

### Auditory brainstem responses (ABRs)

ABR measurements were conducted using a TDT RZ6/BioSigRZ system (Tucker-Davis Tech. Inc., US) in a sound-proof chamber.<sup>70,71</sup> Animals were anesthetized, and the body temperature was maintained near 37°C using a regulated heating pad with a thermal probe placed under the abdomen (Homeothermic Monitoring System, Harvard Apparatus, US). Sound stimuli, which were generated by SigGen RP (Tucker-Davis Tech. Inc., US), were delivered via a speaker (MF1, Tucker-Davis Tech. Inc., US) placed 10 cm away in front of the animal's vertex. ABRs were recorded via three subdermal needle electrodes placed at the animal's vertex (active electrode), left infra-auricular mastoid (reference electrode), and right shoulder region (ground electrode). Signal digitalization and acquisition were done with the software BioSigRZ (Tucker-Davis Tech. Inc., US). The raw signals were amplified (5000x) and bandpass filtered (0.03-5 kHz). The sound level of stimulus started from 90 dB SPL and was decremented in 5 dB steps to ~10 dB below a threshold, which was defined as the lowest stimulus needed for evoking visible responses. ABR-wave-1 amplitudes were measured and computed offline.

### Sample preparation

In each experimental group, two representative mice were chosen based on their ABR threshold shifts and wave-1 amplitudes that are closest to the group means. *En bloc* EM staining of the cochlea was performed following the established protocol.<sup>50</sup> In brief, after being anesthetized with 2% isoflurane inhalation, animals were decapitated, and temporal bones were dissected from both sides. Under the microscope, the cochleae were immediately perfused through the round and oval windows with an ice-cold fixative mixture containing 0.08 M cacodylate (pH 7.4, Sigma-Aldrich, US), 2% paraformaldehyde (Sigma-Aldrich, US) and 2.5% glutaraldehyde (Sigma-Aldrich, US). Post-fixation and sequential decalcification were carried out at 4°C by immersing in the same fixative and with the addition of 5% EDTA (Sigma-Aldrich, US) for 5 hours each. The decalcified cochleae were then washed twice with 0.15M cacodylate buffer (pH 7.4) for 30 min each, followed by sequential immersion in 2% OsO<sub>4</sub> (Ted Pella, US), 2.5% ferrocyanide (Sigma-Aldrich, US), and 2% OsO<sub>4</sub> at room temperature for 2, 2, and 1.5 hours, respectively. All staining solutions were buffered with 0.15M cacodylate buffer (pH 7.4). After being washed with 0.15M cacodylate buffer and nanopore-filtered water for 30 min each, the cochleae were sequentially incubated in 1% freshly made and filtered thiocarbonhydrazide solution (saturated aqueous solution, Sigma-Aldrich, US), 2% OsO<sub>4</sub> aqueous solution and lead aspartate solution (0.03M, pH 5.0, adjusted by KOH) at 50°C for 1, 2 and 2 hours, with immediate washing steps. For embedding, the cochleae were dehydrated through a graded acetone-water mixture (50%, 75%, 90% acetone at 4°C for 30 min each) into pure acetone (3 times at room temperature for 30 min each). Then the dehydrated cochleae were infiltrated with a 1:1 mixture of acetone and Spurr resin monomer (4.1g ERL 4221, 0.95g DER 736, 5.9g NSA, and 1% DMAE; Sigma-Aldrich, US) at room temperature for 6 hours on a rotator, followed by 1:2 mixture of acetone and resin monomer at room temperature for overnight on a rotator. Infiltrated cochleae were then incubated in pure resin for 8-12 hours before being placed in embedding molds (Polyscience, Germany) and incubated in a pre-warmed oven at 70°C for at least 72 hours.

### X-ray microscopy (XRM) and serial block-face EM (SBEM)

For high-resolution XRM imaging of the cochlea, excess resin around the cochlea was carefully removed using a trimmer (TRIM2, Leica, Germany) equipped with a diamond knife head (#227172, Anton Meyer & Co. Ltd). Cochlea samples were mounted upright along the conical center axis on a metal rivet (3VMRS12, Gatan, UK) and scanned with an XRM (Xradia 520 Versa, Carl Zeiss, Germany) at a pixel size of < 4.7 μm, source voltage 60 kV, power 5 W and exposure time per radiograph 1 sec. Cochlear 3D reconstructions based on acquired XRM datasets were visualized and further analyzed in 3D image processing software (AMIRA, Thermo Scientific, US). The whole extent of the basilar membrane was annotated with marked segments of interest using a published cochlear place-frequency map of the mouse as a reference.<sup>72</sup> After

having trimmed the cochleae coronally to the targeted location, we imaged ( $30 \times 30 \text{ nm}^2$ ,  $60 \times 60 \mu\text{m}^2$  per image) the block face of each sample using an SEM (Gemini300, Carl Zeiss, Germany) for *post hoc* confirmation of the frequency range of the SBEM volumes (Figure 1E).

The samples were remounted with the previously scanned block face on top and further trimmed down to a block size of about  $800 \times 800 \times 500 \mu\text{m}^3$  (xyz). Serial sections were imaged using a field-emission SEM (Gemini300, Carl Zeiss) equipped with an in-chamber ultramicrotome (3ViewXP, Gatan) and back-scattered electron detector (Onpoint, Gatan). In total, six SBEM datasets were analyzed in this study (Figure 1F), two (M1 and M2) unexposed cochleae, as well as four (M3-6) noise-exposed cochleae. Imaging parameters were as follows: incident electron beam energy, 2 keV; pixel dwell time, 1.5 - 2.0  $\mu\text{s}$ ; pixel size, 11 - 12 nm; cutting thickness 50 nm; focal charge compensation, 100%; vacuum chamber pressure,  $\sim 2.8 \times 10^{-3}$  mbar. Consecutively acquired slices were aligned offline using a cross-correlation function in MATLAB (MathWorks, US) and cubed for volume tracing.<sup>33</sup>

### Reconstruction of IHC and ribbon synapse

IHCs were reconstructed following a two-step procedure including in-plane probability map prediction and inter-plane connection. First, a previously trained 3D U-net model<sup>31</sup> was utilized with a blocking scheme to predict the IHC binary masks. Specifically, the full-size datasets were cropped into overlapping blocks (block:  $512 \times 512 \times 16$  voxels, overlap:  $128 \times 128 \times 4$  voxels) for parallel running of the computation. The final IHC probability maps were generated by fusing the outcomes of overlapping areas. Then, over-segmented super-pixels for IHCs were obtained by applying a distance-transform-watershed algorithm to thresholded probability maps. Second, a 3D connection algorithm was used to connect the 2D super-pixels and output the reconstructed 3D objects. From all the datasets, 122 IHCs were volume reconstructed. Manual proofreading and correction were done on the auto-segmentation results of IHCs.

### Determination of IHC coronal plane and tilt angle

The coronal plane of each IHC (Figure 3A) was determined by two reference lines, namely the IHC vertical axis computed by principal component analysis (PCA) and the horizontal axis in parallel to the row of IHCs.<sup>31</sup> Through the determined coronal plane, each cell body was divided into pillar and modiolar hemispheres, to which individual ribbon synapses were assigned automatically based on their spatial coordinates. The IHC tilt angle was defined as the angle between the IHC coronal plane and the cuticular plate. To quantify the relative tilt of IHC subtypes (Figure 3B), a virtual middle plane was obtained by the mean tilt angles of manually grouped type-A and type-B IHCs, and then the intersection angles between the middle plane and IHC coronal planes were measured in each dataset. Positive and negative values were defined arbitrarily for cell bodies below and above the middle plane, respectively.

### Measurement of ribbon and mitochondrion

In all reconstructed IHCs, ribbon synapses were manually annotated and volume traced using a browser-based image data analyzing tool (webKNOSSOS).<sup>69</sup> For quantifying the postsynaptic mitochondrial content (Figures 4B–4D), five type-A and five type-B IHCs were randomly selected from each dataset. Onto those 60 IHCs, 945 SGN terminals were identified, and they were divided into pillar and modiolar groups according to their associated ribbon synapse positions. Mitochondria were manually annotated within the SGN terminal region, which was defined as varicosity at the nerve ending. In total, 5649 mitochondria were identified and classified based on their size and morphology as small (sphere), medium (ellipsoid), and large (complex form).

## QUANTIFICATION AND STATISTICAL ANALYSIS

All data analysis and statistical tests were carried out using self-written scripts and built-in functions in MATLAB (release 2021a) and the Statistics Toolbox (MathWorks, Inc., US). The means comparisons between groups were done using the paired-sample t test (*ttest*) for Figure 1C and the two-sample t test (*ttest2*) for Figures 1B, 3B, S2A, and S2B. The medians comparisons between groups were done using the Wilcoxon rank-sum test (*rank-sum*) for Figures 3D–3F and 4B–4D. The distribution comparisons between groups were done using two-sample Kolmogorov-Smirnov tests (*kstest2*) for Figures 2B–2D, 3C, 4E, 4F, and S3A–S3F. The comparison between groups was done using one-way analysis of variance (*anova1*) for Figure 3B. The significance level of statistical tests was denoted as n.s. for  $p > 0.05$ , \* for  $p < 0.05$ , \*\* for  $p < 0.01$ , \*\*\* for  $p < 0.001$ , and \*\*\*\* for  $p < 0.0001$ .